Mechanical characterization of shale matrix minerals using phase-positioned nanoindentation and nano-dynamic mechanical analysis

Chao Yang[a], Yongqiang Xiong[a,*], Jianfeng Wang[a,b], Yun Li[a], Wenmin Jiang[a]

[a] *State Key Laboratory of Organic Geochemistry, Guangzhou Institute of Geochemistry, Chinese Academy of Sciences, Guangzhou 510640, PR China*
[b] *University of Chinese Academy of Sciences, Beijing 100049, PR China*

ABSTRACT

The accurate determination of mechanical parameters (namely, Young's modulus and hardness) of shale-constitutive minerals is crucial for predicting the macroscale mechanical parameters of shale composites. This study employed an advanced nanoindentation apparatus equipped with a high-resolution microscope ($4000\times$) and a newly emerging nano-dynamic mechanical analysis (nano-DMA) module to conduct mineral-positioned indentation and investigate the depth profiles of mechanical parameters of shale matrix minerals, with the objective of obtaining their intrinsic mechanical values. To conduct mineral-positioned nanoindentation, various matrix minerals were pre-discerned under the optical microscope based on their particle shapes, surface features, and reflection colors. The mechanical response curves show that silicates (quartz and feldspar) exhibit significant elastic characteristics, whereas carbonates (dolomite and calcite) and clay minerals exhibit a combined deformation behavior of elasticity and plasticity based on the elastic recovery ratio and plastic work ratio. The mechanical depth profiles produced by nano-DMA show that the mechanical parameters of all aforementioned minerals decrease rapidly with respective to the increase in indentation depth, before reaching stable values. This variation pattern for the mechanical parameters is a result of the indentation size effect (ISE), which comes from the internal structure (or texture) adjustment of the indented material in small deformed volumes during indenter invasion. Whereas the platform section represents the indenter overcoming the ISE layer and actually probing the material as it is, the mechanical values measured at this stage can be recognized as the true values for the indented materials. In addition, the tested mineral grains would be easily affected by the substrate phases at a much larger indentation depth, and the mechanical parameters would correspondingly change in the mechanical depth profiles after the plateau stage. Overall, our findings identify reliable Young's moduli and hardnesses for different matrix minerals: 30 GPa and 1.5 GPa for clay minerals, 105–110 GPa and 14–16 GPa for quartz, 75–85 GPa and 9–10 GPa for feldspar, 70–75 GPa and 2–3 GPa for calcite, and 115–120 GPa and 7–8 GPa for dolomite.

1. Introduction

Shale gas development can be practically realized via horizontal drilling and hydraulic fracturing techniques (Carter et al., 2011; Blackwill and O'Sullivan, 2014). The successful use of these techniques relies heavily on a understanding of shale mechanical properties (Nagel et al., 2012; Alkharraa et al., 2015). Shale is a fine-grained sedimentary rock consisting of a mixture of various minerals and a small quantities of organic matter, among which the minerals constitute the pressure-burden framework of the shale. Therefore, correct understanding of the mechanical responses of shale-constitutive minerals to external forces and accurate determination of their mechanical parameters are crucial for understanding and predicting the macroscale mechanical properties of shale composites.

Conventional macroscale mechanical testing techniques such as uniaxial/triaxial compression testing, cannot be used to measure the elastic modulus of micrometer-scale minerals in a shale matrix. Thus, in recent years, researchers have creatively introduced nano-indentation technology into the characterization of the micromechanical properties of shale composites and their constituents (e.g., Bobko and Ulm, 2008; Kumar et al., 2012; Bennett et al., 2015; Abedi et al., 2016; Liu et al., 2016, 2018, Liu and Mehdi, 2017; Yang et al., 2016; Li et al., 2019; Manjunath and Jha, 2019; Shi et al., 2019). However, despite these advances, the mechanical properties of minerals in a shale matrix have not been fully studied or lack accurate characterization, rendering the determination of macroscale mechanical parameters of shale and

* Corresponding author.
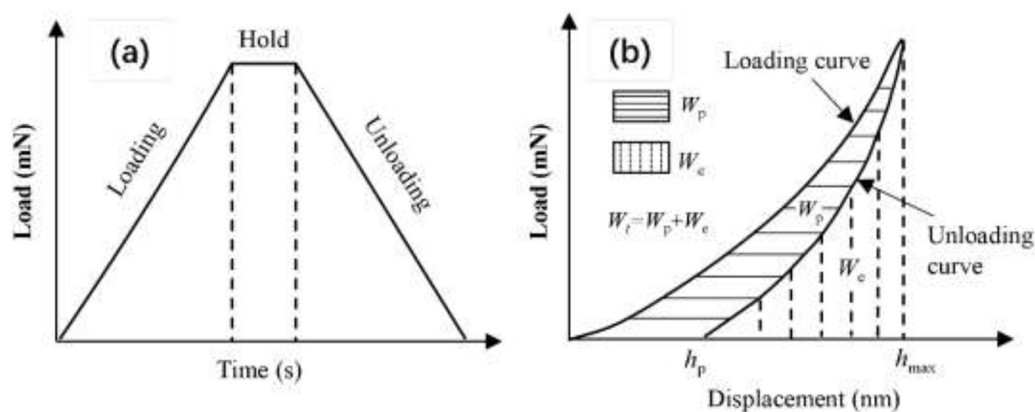 *E-mail address:* xiongyq@gig.ac.cn (Y. Xiong).

Fig. 1. Plot of variation of applied load with time (a) and schematic of the typical nanoindentation curve (b). h_{max}: the maximum indentation depth during indentation. h_p: the residual indentation depth after the indenter retract from the sample surface. We: the elastic work. Wp: the plastic work. Wt: the total work.

prediction of seismic velocity challenging.

Nanoindentation technique uses a diamond indenter with known shape and mechanical parameters to press into a sample surface using a load in millinewtons (Oliver and Pharr, 1992; Schuh, 2006). In nanoindentation testing, the indentation depth is the most important technical parameter because indentation tests using various depths probe different volumes, and thus, produce different mechanical responses (Fischer-Cripps, 2002). Previous shale nano-indentation practices used small indentation depths (hundreds of nanometers) to measure the mechanical parameters of shale constituents. The choice of indentation depth in such studies is based on the principle that the volume affected by an indenter was small enough not to mechanically interact with other phases. Whereas this assumption is theoretically reasonable, the assigned indentation depths are lacking in data support showing the correlation of mechanical parameters with indentation depth, from which we can identify the true mechanical values of the indented minerals.

Additionally, in the past, phase-positioned mechanical testing in a heterogeneous composite material was difficult to perform because the optical microscope provided in the indentation apparatus had a low resolution. Therefore, in previous studies, researchers generally used the statistical nanoindentation method to determine the mechanical parameters of shale constituents (Akono and Kabir, 2016; Liu et al., 2018; Mashhadian et al., 2018; Zhang et al., 2018; Li et al., 2019). This method consists of a primary task of obtaining significant quantities of indentation data through grid indentation, followed by the extraction of the mechanical parameters of each phase using a Gaussian distribution model (Ulm et al., 2003; Constantinides et al., 2006; Zhu et al., 2007). In theory, this model can distinguish the mechanical parameters of all single phases in a heterogeneous composite. However, there are many uncertainties with this model when applied to highly heterogeneous shales containing more than five phases with different volume portions and particle sizes. Thus, in most cases in previous studies, only phases with high volume fraction in the shale were assigned their mechanical values.

In view of omissions and defects in the mechanical characterization of shale matrix minerals using the nanoindentation technique, it is necessary to conduct mineral-positioned indentation and quantitatively investigate the correlation between mechanical parameters and indentation depth. In this study, an Anton Parr TTX NHT³ indentation apparatus, equipped with a high-resolution optical microscope (maximum 4000×), was used for the nanoindentation testing. Such a high-resolution microscope can clearly distinguish the micrometer-scale minerals in shale matrix, thus enabling phase-positioned indentation. The apparatus is also equipped with a newly emerging nano-dynamic mechanical analysis (nano-DMA) module, which can determine the

elastic modulus and hardness as a continuous function of indentation depth in a single load cycle, thus helping in the determination of intrinsic mechanical parameters of shale-constitutive minerals.

It should be noted that some researchers in recent years have started to use PeakForce Quantitative Nanomechanical mapping mode (PeakForce QNM), a proprietary mode for use in atomic force microscopy (AFM), to characterize the elastic moduli of shale constituents (Eliyahu et al., 2015; Emmanuel et al., 2016; Yang et al., 2017a; Li et al., 2018). This technique applies a constant peak force at the nanonewton scale, allowing the tip to sense a nano change in volume, and thereby quantitatively map nanoscale mechanical parameters of organic matter (OM) (Pittenger et al., 2014). However, despite its high mechanical resolution, there is a limited range of moduli (generally within 100 GPa) owing to its inherent flaws, such as a low cantilever spring constant (DNISP; Bruker; spring constant 300–650 N/m). Additionally, the AFM QNM technique has significant errors compared with nanoindentation testing when measuring materials with high modulus. Trtik et al. (2012) reported a measurement error with an estimated uncertainty of up to 15% for materials with elastic modulus higher than 40 GPa. Additionally, the peak force used in AFM QNM is extremely small that it cannot depict the mechanical responses of materials under external stresses. Moreover, the AFM QNM measures the elastic moduli of materials without producing any hardness data. For the application scope of AFM QNM, nanoindentation is therefore still necessary for characterizing the mechanical responses of shale matrix minerals.

2. Materials and experiments

2.1. Instrumented nanoindentation technique

2.1.1. Dynamic nanoindentation technique

In this section, prior to the introduction of the dynamic nanoindentation technique, the previously used conventional quasi-static nanoindentation technique is briefly discussed. The methodology and operating principle for the nanoindentation technique have been reviewed and presented in detail elsewhere (Oliver and Pharr, 1992). Indentation testing involves making contact between a sample and an indenter tip of known geometry and mechanical properties. Typical tests consist of a constantly increasing load, followed by a short hold and then continue with a constant unloading procedure (Fig. 1a).

The load (P) and displacement (h) are monitored continuously during the indentation process, resulting in a load–displacement curve, as shown in Fig. 1b. The loading stage can be considered as a combination of elastic and plastic deformations whereas the unloading stage can be considered as a recovery mode for pure elastic deformation.

Correspondingly, the areas underneath the loading curve and unloading curve are the total work W_t done by loading and elastic work W_e released by unloading, respectively. Therefore, the areas enclosed by the loading-unloading curves is the (plastic) work done by the indentation process, calculated as $W_p = W_t - W_e$.

Typically, mechanical property extraction is achieved through the use of a resultant *P–h* unloading curve and through the application of a continuum scale model to derive a reduced elastic modulus, E_r:

$$E_r = \frac{\sqrt{\pi}}{2\alpha} \frac{S}{\sqrt{A_c}} \tag{1}$$

$$H = \frac{P_{max}}{A_c} \tag{2}$$

where $S = \frac{dP}{dh}$ is the initial slope of the unloading branch of the *P–h* curve and represents the stiffness of the material, α is a constant related to the geometry of the indenter (α =1.034), and A_c is the projected contact area of the indenter on the sample surface. The projected contact area, A_c, is typically determined as a function of the maximum indentation depth, h_{max} (Oliver and Pharr, 2004).

In dynamic indentation, on the other hand, the sinusoidal oscillating component (Eq. (3)), is superimposed onto the quasi-static loading applied to the sample, producing measurable displacement oscillations (Eq. (4)). A typical example of the sinusoidal force and the corresponding displacement is shown in Fig. 2. The contact stiffness can be expressed in terms of oscillating component and other measurable or known properties of the system by applying an appropriate rheological model for the indenter-sample system (Eq. (5)). Because the contact stiffness can be obtained at every point of the loading–unloading cycle, the hardness and reduced modulus are therefore calculated as a continuous function of depth according to the Eqs. (1)-(2).

$$P_{(t)} = P_0 e^{i\omega t} \tag{3}$$

$$h_{(t)} = h_0 e^{i(\omega t + \varphi)} \tag{4}$$

$$S = \left[\frac{1}{\frac{P_0}{h_o} \cos\varphi + m\omega^2 - k_s} - \frac{1}{k_f} \right]^{-1} \tag{5}$$

where h_0 is the displacement amplitude. P_0 is the excitation load amplitude. ω is the angular frequency in radians/s. φ is the phase angle of displacement lag load. k_s and k_f are the stiffness coefficients of the sample and the indenter frame.

Furthermore, the reduced modulus acquired through indentation inherently includes the elastic properties of both the test and indenter materials (Oliver and Pharr, 1992). Based on knowledge of the reduced modulus and Poisson's ratio, the Young's modulus of the indented material can be calculated as follows:

$$\frac{1}{E_r} = \frac{(1 - \nu^2)}{E} + \frac{(1 - \nu_i^2)}{E_i} \tag{6}$$

where ν_i and E_i are the Poisson's ratio and Young's modulus, respectively, of the indenter. For diamond, E_i =1140 GPa and ν_i = 0.07. Meanwhile, ν and E are the Poisson's ratio and Young's modulus, respectively, of the indented materials. In this study, the Poisson's ratios of common minerals in shale are assigned classic values based on previous literature; for example, the Poisson's ratios of quartz, feldspar, calcite, dolomite, and clay mineral are 0.06, 0.26, 0.28, 0.29, and 0.3, respectively (Bass, 1995; Mavko et al., 2009).

2.1.2. Instrument and experimental parameters

In this study, the TTX NHT[3] indentation apparatus, manufactured by Anton Paar, was employed for the nanoindentation testing (Fig. 3). This instrument consists mainly of three parts: an indentation system equipped with a Berkovich indenter (three-sided pyramidal diamond tip with a radius of curvature of 150 nm), an optical microscope with a maximum magnification of 4000×, and a sample transportation platform with a 50 nm site selection resolution. The optical microscope, together with an automated stage, allows location selection of the position to be indented. Following the determination of areas of interest, the nanoindentation system employs an electro-mechanical actuator to create an indent into the specimen and capacitive displacement sensors to measure the depth of penetration. The maximum load of the instrument is 500 mN. The resolutions of the displacements and loads are 0.01 nm and 20 nN, respectively. In addition, to reduce the disturbance due to ambient environment and noise, the instrument is equipped with a damping table and an acoustic enclosure.
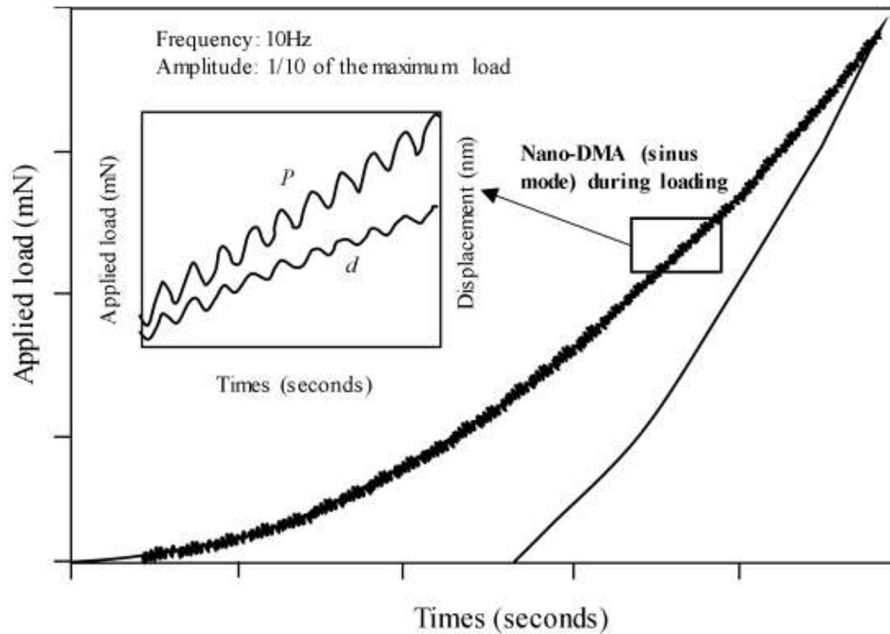

Fig. 2. Measurement made with the Anton Parr instruments sinus mode showing the load-depth plot together with a zoomed portion of the loading curve where the force sinus (P) can be seen superimposed on the resultant displacement signal (d).
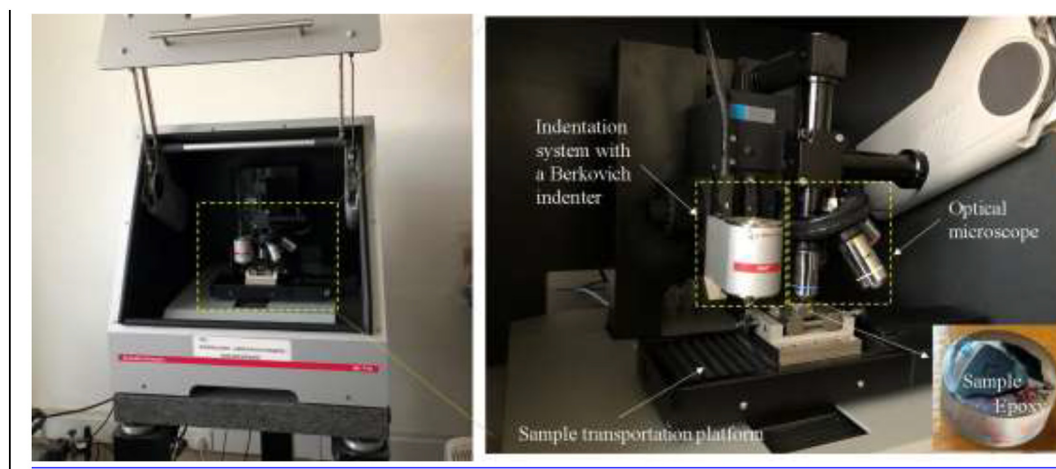
Fig. 3. TTX-NHT3 indentation instrument illustrating the major components and the testing shale sample embedded into epoxy.

Before indentation was performed on a shale sample, the tip was calibrated via experiments on a fused quartz standard using quasi-static nanoindentation. The calculated Young's modulus for fused silica was 74 ± 0.5 GPa, which is very nearly equal to the literature value of 75 ± 2 GPa. The same fused silica specimen was also used as a calibration standard to check the reproducibility and consistency of the measurements. For all indentation tests, the indenter was set to approach and retract from the surface of the sample at a rate of 2000 nm/min within a vertical distance of 2000 nm from the sample surface.

In this study, the nano-DMA was used during the loading period. The loading was conducted with a frequency of 10 Hz and a load amplitude of 1/10 of the maximum load. When the maximum load was reached, the load was held for a period of 2 s and then unloaded in 30 s. The nano-DMA mode is also called the sinus mode in the Anton Paar nanoindentation devices.

2.2. Shale materials and preparation

2.2.1. Shale material

A shale core sample, collected from the marine Lower Silurian Longmaxi Formation in the Sichuan Basin, China, at a depth of 89 m, was selected for the nanoindentation testing. The X-ray diffraction results indicate that the sample was composed of quartz and clay minerals at 34.4% and 45.9%, respectively (Table 1). In addition, the sample contains various other minerals: feldspar (13.6%), calcite (1.8%), dolomite (2.7%), and pyrite (1.5%). Organic geochemical analyses show that the total organic carbon (TOC) content of the sample was 3.4 wt% and that the calculated equivalent vitrinite reflectance was 2.9%, suggesting an overmature stage.

2.2.2. Sample preparation

A plane/smooth sample surface perpendicular to the indenter is necessary for the test, to obtain reliable measurements. In this study, the selected shale sample cored perpendicular to the bedding plane direction was cast into epoxy (Fig. 3) to simplify the process of surface polishing by a surface preparation machine. Grinding and polishing were performed using rotating disks mounted with emery paper of various grit sizes gradually transitioning from 50 to 2000 grit size. The

epoxy resin was then finely polished using 6 μm diamond suspension polishing fluid, followed by a 1.0 μm diamond suspension polishing fluid, and finally a 50 nm colloidal silica suspension.

Fig. 4 a–b shows the surface morphology of the sample after mechanical polishing, wherein the surfaces of the hard phases are very flat, and the soft phases cannot be focused concurrently. This indicates that the hard phases (silicate, carbonate, and iron minerals) in shale matrix can be polished easily, whereas soft phases (organic matter and clay minerals) tend to get pulled out. Because of this phenomenon, electrochemical polishing was employed to reduce the surface height difference between the soft and hard phases, allowing the surface of softer phases to be polished. In particular, the sample was polished in an IM4000 argon ion mill produced by Hitachi High-Tech Global Corporation under a 4.0 kV intensity at a 5° angle for 2 h. Fig. 4c–d shows the sample surface after ion polishing, wherein the phases in the matrix are nearly in the same height plane.

3. Results and discussion

3.1. Identification of shale constituents under optical microscope

To conduct the phase-positioned nanoindentation, the matrix minerals must be pre-identified under the optical microscope. Shale constitutive minerals can be divided into four categories: iron sulfides (such as pyrite), carbonate minerals (calcite and dolomite), silicate minerals (quartz and feldspar), and the clay minerals. Because different minerals have different morphological and optical characteristics, a combination of particle shapes and reflection characteristics observed under the optical microscope can help distinguish the shale matrix minerals.

In the Longmaxi shale, pyrite, which has a very high reflection intensity and exhibits a bright white color in incident light under the microscope, is the predominant iron-mineral type (Fig. 5a). It generally occurs in the form of framboidal clusters, the length scale of which is on the order of 1–8 μm. Notably, the monocrystalline within a cluster is generally less than 400 nm, as revealed in previous studies using scanning electronic microscopy (SEM) (Zhao et al., 2017; Yang et al., 2020), which is beyond the resolution of the optical microscope. It is for this reason that we did not conduct nanoindentation tests on pyrite.

Dolomite grains are of a weak whitish color in incident light under the optical microscope (Fig. 5b), and generally exhibit an approximate rhombohedral shape, the intrinsic crystalline form of carbonate minerals. They are usually very large, ranging in size from 20 to 50 μm. Under the microscope, calcite grains, on the other hand, are relatively darker than dolomites because the calcite crystal is translucent and therefore absorbs some of the incident light (Fig. 5c). Additionally,

Table 1
Shale sample information used for nanoindentation testing.

Depth (m)	Organic parameters		Mineralogical compositions				
	R_o (%)	TOC (wt%)	Clay	Quartz	Feldspar	Carbonate	Pyrite
89	2.9	3.4	34.4	45.9	13.6	4.5	1.5
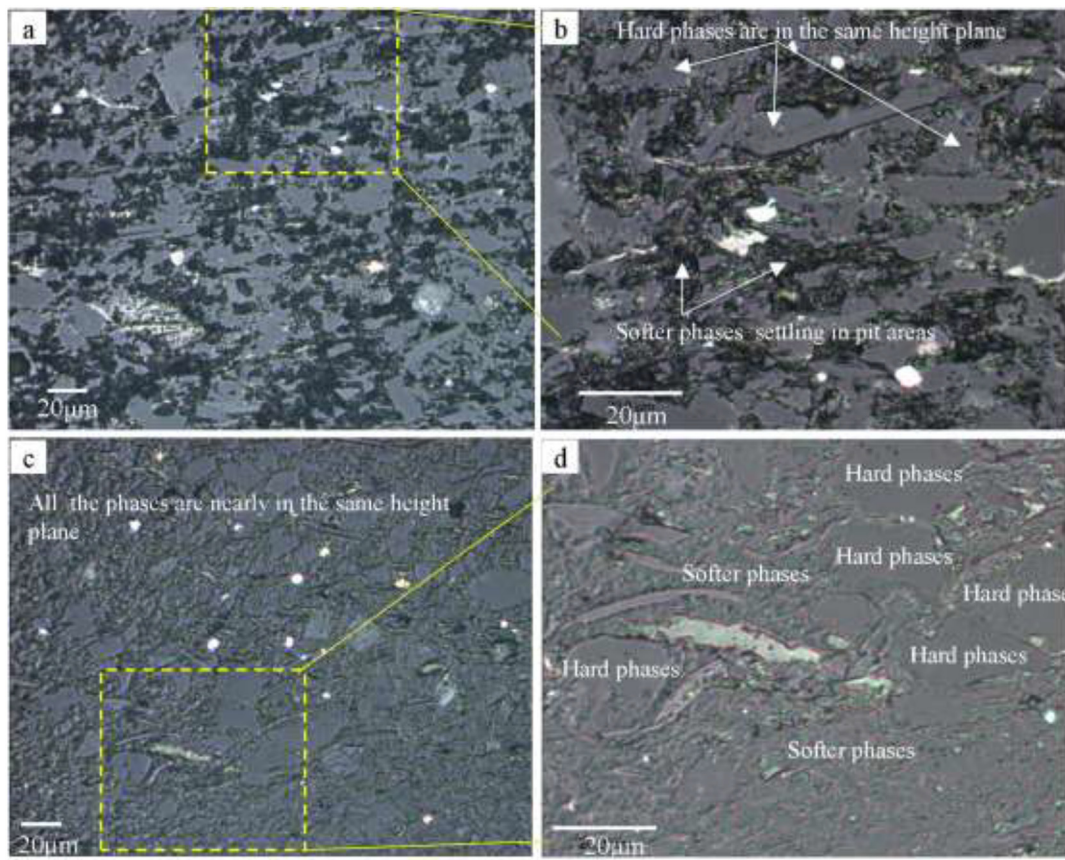
Fig. 4. The surface morphology of shale rock slices under optical microscope after mechanical polishing (a–b) and subsequent ion polishing (c–d). (a–b) The surfaces of the hard phases are in the same height plane, and the soft phases cannot be focused concurrently. (c–d) All phases in shale matrix are nearly in the same height plane. Note: (a) and (c) were shot with 20× objective lens, (b) and (d) were shot with 50× objective lens, and the magnification of eyepiece is 20 × .

calcite grains are relatively smaller than dolomites and generally do not exhibit a rhombic crystalline shape. Notably, the mechanically polished carbonate minerals (especially the calcite) usually exhibit regularly spaced stripes on the surface (Fig. 5b–d), which is a significant morphological feature different from those of other minerals.

Quartz crystals are translucent, thus displaying a dark gray color in incident light (Fig. 5d). They have large grain sizes, mostly in the range of 15–40 μm, and exhibit various irregular shapes with straight and sharp edges. Notably, mechanically polished quartz grains have the smoothest and cleanest surfaces, which is a distinct morphological feature that distinguishes them from other minerals (Fig. 5d). It should also be noted that previous studies have revealed the existence of certain amounts of fine-grained quartz particles (less than 2 μm) in various marine and lacustrine shales (e.g., Milliken et al., 2016; Dong et al., 2019, Dong and Harris, 2020; Yang et al., 2020), which however cannot be identified under an optical microscope because of a very faint color contrast with the surrounding dark gray minerals.

Transparent feldspar crystals are also dark gray in incident white light and, in most cases, manifest as large columns or plates, which is the characteristic crystalline form of feldspar-group minerals (Fig. 5d). Additionally, mechanically polished feldspar has a very smooth surface. However, this surface is often mixed with impurities, which makes it not as clean as the surface of quartz (Fig. 5e). It should be noted that granular feldspar can be either orthoclase or plagioclase, but it is difficult to distinguish them under reflected light. For this reason, in this study, the indentation testing of feldspar does not distinguish between the orthoclase and plagioclase.

Clay minerals are easily identifiable under the optical microscope. They settle in pit areas and cannot be recognized as entities under the mechanically polished rock slice (Fig. 4a–b and Fig. 5a–e), whereas

they expose a fine-grained texture without distinct crystalline forms after the subsequent ion polishing processes (Fig. 4c–d and Fig. 5f). The fine-grained texture is essentially the result of dense stacking of individual plate-like clay particles with thicknesses of tens of nanometers (Wilson et al., 2016a; Wilson et al., 2016b). Overall, clay minerals are continuously distributed, acting as a framework material with other mineral grains embedded in it. It is noteworthy that wherever clay particles are observed, fine-grained organic materials are found to be interspersed within them (Fig. 5f). The organic matter is off-white, consistent with observations under oil-immersed whole-rock slices in organic petrology studies (Hackley and Cardott, 2016).

Although there are still some shortcomings of this identification method, such as the inability to distinguish the feldspar subclasses and recognize the fine-grained quartz particles (less than 2 μm), it overall meets the requirements for phase-positioned indentation of the shales.

3.2. Indentation responses of matrix minerals

Based on mineral identification, representative shale constitutive minerals with characteristic length scales of approximately 20–40 μm are selected for nanoindentation testing. Figs. 6–10 show the resultant load–displacement curves at various indentation loads and the corresponding indent imprints imaged by the optical microscope. The corresponding indentation data are listed in Table 2.

The indentations on quartz (curves in Fig. 6a–b, and optical images in Fig. 7a–b) and feldspar grains (curve in Fig. 6c–d, and optical images in Fig. 7c–d) result in similar load-displacement curves. The curves each have a low unloading slope and a small irrecoverable deformation. Consequently, this results Ain a series of very narrow hysteresis loops enclosed by the loading–unloading curves, indicating that the
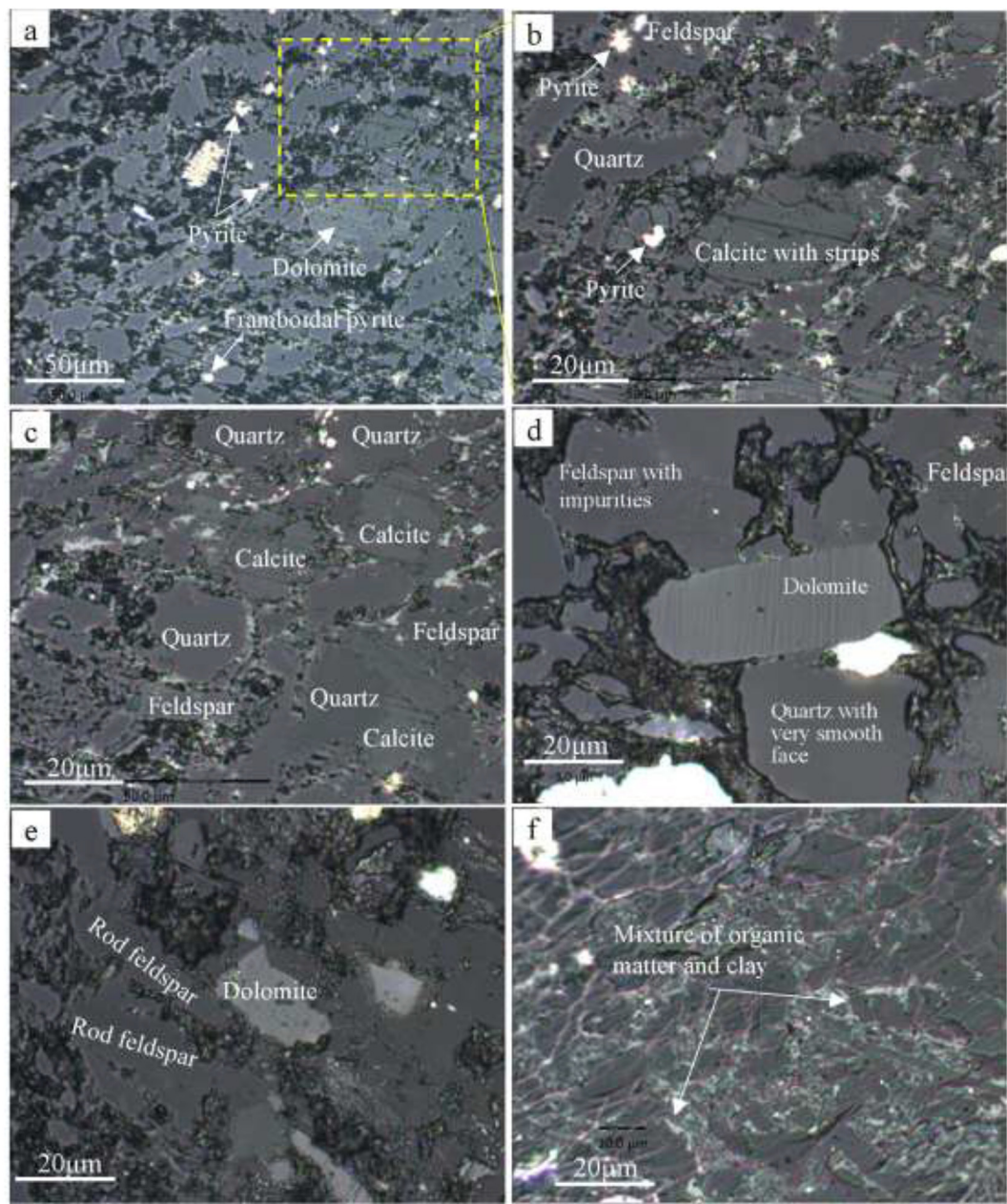
Fig. 5. The identifying characteristics of different matrix minerals using the optical microscope. (a) Pyrite has a very high reflection intensity and exhibits a bright white color. (b) Dolomite grain is of a weak whitish color and exhibits an approximate rhombohedral shape with spaced stripes on the surface. (c) Calcite grains are relatively darker than dolomites and generally have various shapes with spaced stripes on the surface. (d) Quartz and felspar grains display a dark gray color, and the latter exhibit various irregular shapes with straight and sharp edges, whereas the former generally manifest as large columns and plates. (e) The felspar grains often show impurities on the surface, while the quartz grains have a very smooth surface. (f) Clay minerals are produced as an aggregates in shale matrix and are usually intermixed with the fine-grained organic matters.

indentation process is dominated by elastic work. The h_p/h_{max} (elastic recovery ratio) and W_p/W_t (plastic work ratio) are in the range of 0.2–0.4 and 0.2–0.5, respectively, quantitatively demonstrating the above inference. Notably, the similar load–displacement curves between the quartz and feldspar with a similar tectosilicate framework indicate that the mechanical responses of minerals are more likely determined by their crystal structures. Additionally, the maximum indentation depth of feldspar that resulted under the same load is larger than that of quartz, which reveals that the quartz is stiffer than the feldspar. Feldspar is formed by replacing a quarter of the Si^{4+} in the quartz crystal structure unit with Al^{3+} and filling some metal ions (Na^+, K^+) to maintain coordination balance. The length of Al−O bond is different from that of Si−O bond, so the replacement of Si^{4+} by Al^{3+}

forms a less stable crystal structure, thus making the strength and stiffness of feldspar being weaker than that of quartz.

In contrast to those of silicate minerals, responses associated with indentation on calcite (curves in Fig. 8a–b, and optical images in Fig. 9a–b) and dolomite (curves in Fig. 8c–d, and optical images in Fig. 9c–d) provide distinctly different load–displacement curves, each with a high unloading slope and a large irrecoverable deformation. Correspondingly, large hysteresis loops are produced by the loading and unloading curves, indicating that the indentation process includes a certain amount of elastic work and a large amount of plastic work. The h_p/h_{max} and W_p/W_t are in the range of 0.5–0.7 and 0.6–0.8, respectively. Notably, the similar load–displacement curves of calcite and dolomite, which have similar crystal structures (Liebau et al., 1986),
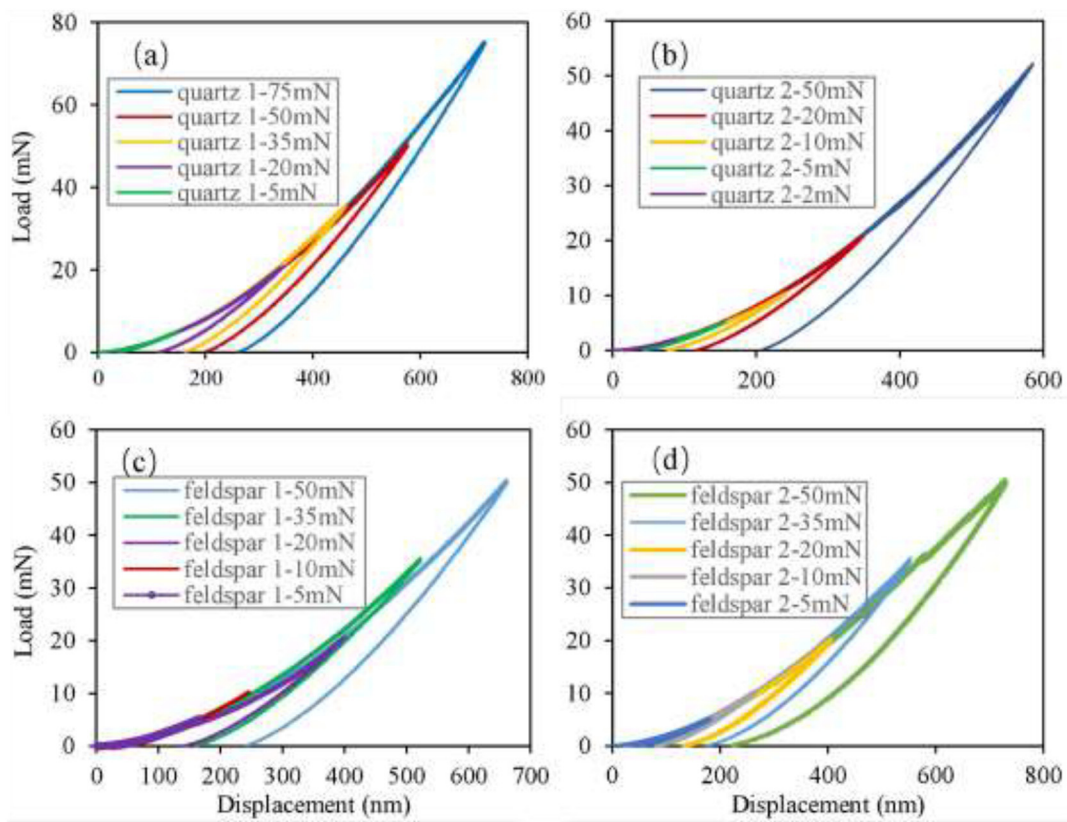
Fig. 6. The group of resulted load-displacement curves of quartz (a–b) and feldspar (c–d) at various indentation loads.
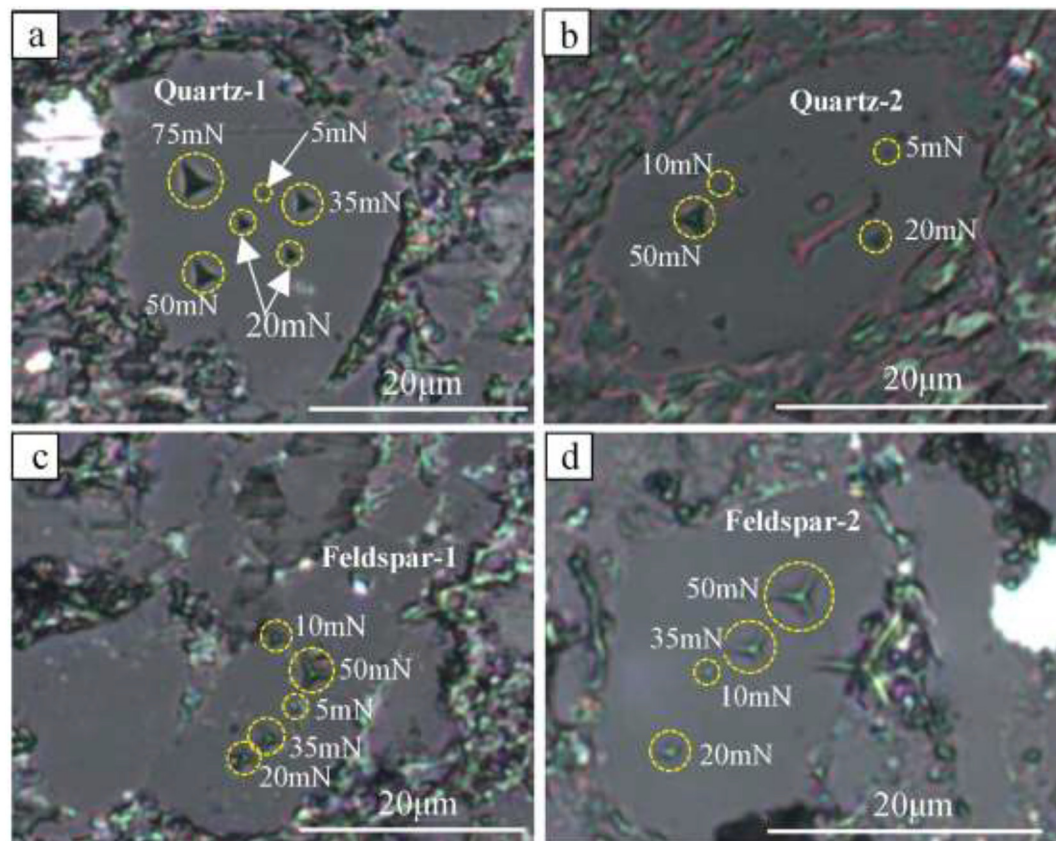

Fig. 7. The corresponding indent imprints of quartz (a–b) and feldspar (c–d) resulted by various indentation loads.
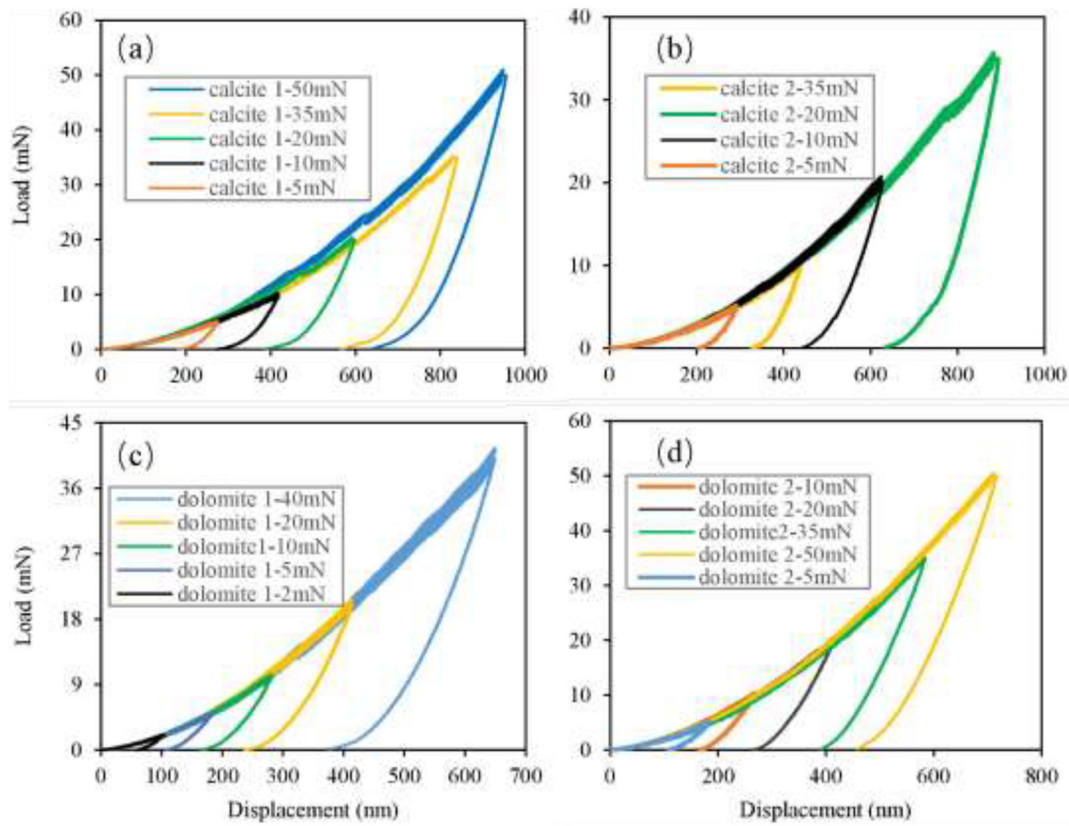
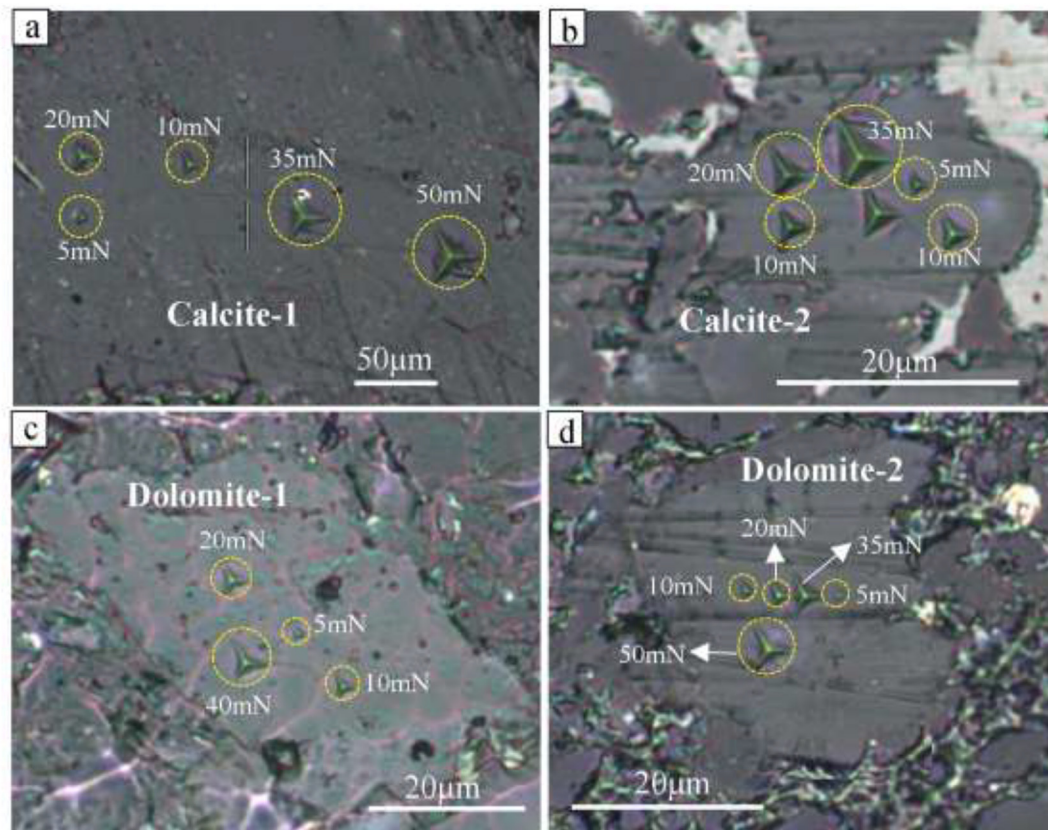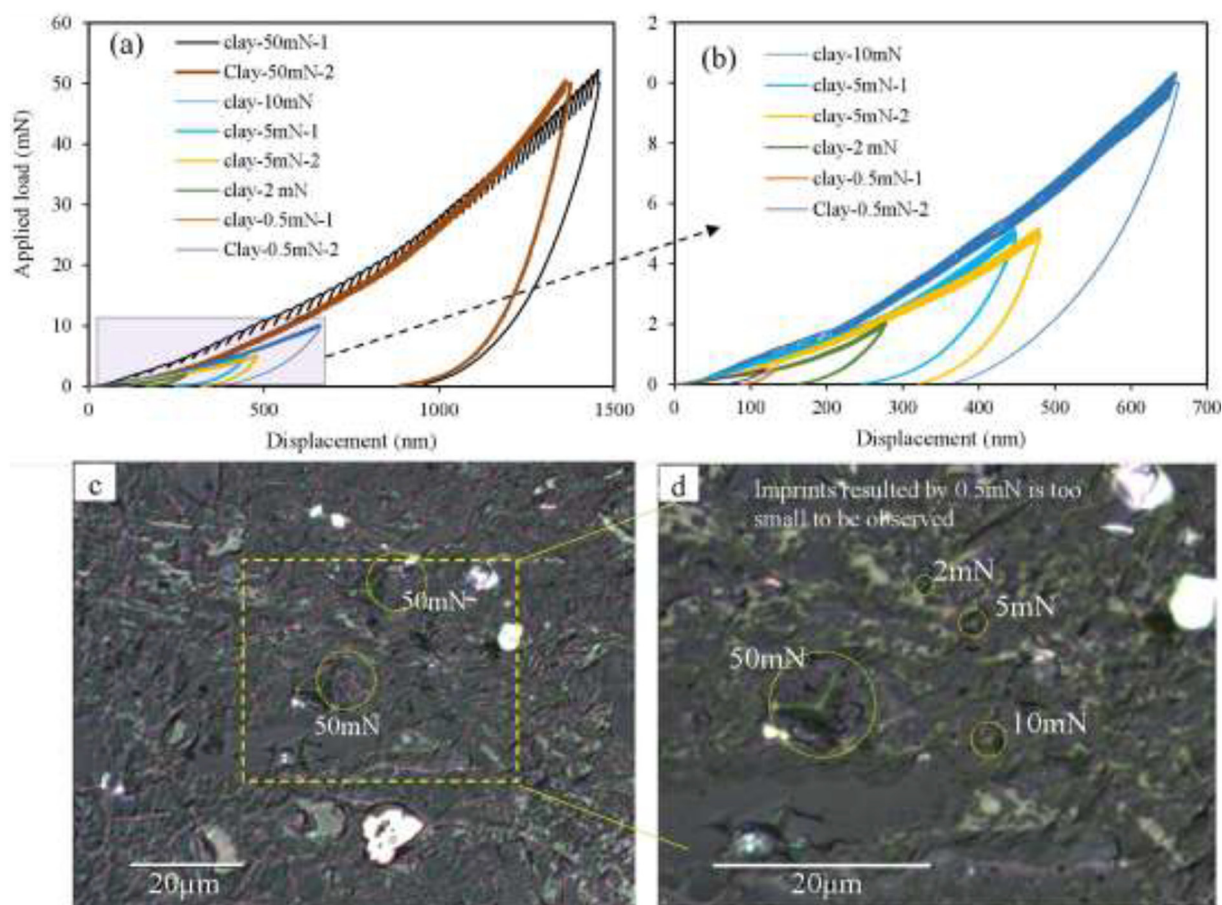**Fig. 8.** The group of resulted load-displacement curves of calcite (a–b) and dolomite (c–d) at various indentation loads.

Fig. 9. The corresponding indent imprints of calcite (a-b) and dolomite (c-d) resulted at various indentation loads.

Fig. 10. The group of resulted load-displacement curves (a–b) of clay minerals at various load and the corresponding indent imprints (c–d) imaged by the optical microscope. (b) is the close-up view of the shaded panel in (a), showing the indentation response curves at various indentation loads less than 10 mN. (d) is the close-up view of the panel in (c), showing the residual imprints resulted by indentation loads less than 10 mN.

prove that the mechanical responses of minerals depend on their crystal structures. Comparatively, the maximum indentation depth of dolomite under the same load is smaller than that of calcite, indicating a greater stiffness for dolomite. Given the different constitutive cations in calcite (Ca) and dolomite (Ca, Mg), the difference in their stiffnesses more likely originated from differences in the species of cations, which have various bond energies to anions (CO_3^{2-}), and may also alter the basic crystalline structures of the minerals to some degree.

The indentation response associated with clay minerals (curves in Fig. 10a, and optical image in Fig. 10b) is similar to that of the carbonate minerals. The curves show a very high unloading slope and exhibits significant irrecoverable deformation. This results in a series of large-belly hysteresis loops enclosed by the loading and unloading curves, indicating that the indentation process is predominated by plastic work. The calculated h_p/h_{max} and W_p/W_t are in the range of 0.6–0.7 and 0.7–0.8, respectively. The significant plastic work ratio of the clay minerals during indentation is due to nanoindentation testing actually sensing the clay composites, whose mechanical properties are determined mainly by the mechanical interactions of contact between individual plate-like clay particles (Bobko and Ulm, 2008; Kuila and Prasad, 2013). When stress is applied, relative displacement occurs between the individual clay particles, making them bend and slip without producing internal stress. Therefore, when the external force is removed, there is not enough internal force to cause the layers to return to their original position, resulting in significant plastic deformation. Additionally, clay minerals are determined to be the softest substance among the shale matrix minerals because they have the largest indentation depth under the same load.

3.3. Mechanical depth profile of matrix minerals

Fig. 11 presents the mechanical depth profiles of shale matrix minerals using nano-DMA. It shows that the mechanical parameters of clay minerals exhibit a two-stage change, i.e., an initial sharp decline, followed by a plateau, with respect to increase in indentation depth. For the non-clay minerals, the variations in their mechanical parameters exhibit one more stage after the plateau: a slow decrease.

The sharp decline in mechanical parameters in the first stage with respect to increasing indentation depth is a typical manifestation of the indentation size effect (ISE), a universal nanoindentation phenomenon known in materials science. In the nanoindentation of crystalline and polymeric materials, the origin of ISE is assumed to be related to the geometrically necessary dislocations (GNDs) that exist in small deformed volumes under the penetration of an indenter (Nix and Gao, 1998; Elmustafa and Stone, 2003; Pharr et al., 2010; Liu et al., 2019), the density of which is proportional to the inverse of the indentation depth. Accordingly, the measured mechanical parameters will decrease with the increase of indentation depth as a result of the decrease in GNDs density. In this way, the GNDs density would be miniscule at a certain large indentation depth, when the indenter really probes the material as it is and thus measures its intrinsic mechanical values. In this study, the threshold indentation depth was about 200–300 nm for the matrix minerals. Because mechanical parameters are inherent properties of the materials, the measured values are supposed to be unchanged after the indenter exceeds the ISE layer, manifested as a plateau in the mechanical depth profile. It should be noted that the clay minerals in shale are outputted as composite materials formed by

Table 2
Indentation data related to the testing shale matrix minerals.

F_m (mN)	h_{max} (nm)	h_p (nm)	h_p/h_{max}	W_{elast} (pJ)	W_{plast} (pJ)	W_{total} (pJ)	Wp/Wt	E_s (GPa)	H_s (GPa)
Quartz-1									
20	337.80	107.05	0.32	1882.94	1559.07	3442.01	0.45	109.38	15.78
5	146.29	26.50	0.18	231.05	154.75	385.80	0.40	131.84	21.17
35	459.15	164.53	0.36	4410.05	2245.49	6655.54	0.34	106.84	15.84
50	576.34	187.51	0.33	7947.30	3315.53	11262.82	0.29	96.71	14.32
75	721.30	259.84	0.36	14557.15	6025.95	20583.10	0.29	94.51	13.56
Quartz-2									
2	85.10	12.43	0.15	58.62	11.45	70.07	0.16	143.87	24.58
5	153.08	29.43	0.19	233.29	58.55	291.84	0.20	122.96	17.63
10	236.79	61.26	0.26	675.88	236.32	912.20	0.26	107.58	14.99
20	342.95	109.72	0.32	1922.98	912.49	2835.48	0.32	106.21	15.22
50	574.79	198.47	0.35	7710.63	3073.90	10784.52	0.29	99.35	13.71
Feldspar-1									
20	394.93	123.40	0.31	2096.84	1734.45	3831.29	0.45	78.84	9.22
5	162.40	26.06	0.16	287.51	130.17	417.69	0.31	99.14	17.75
35	520.84	145.79	0.28	5281.90	2298.94	7580.84	0.30	80.48	11.17
50	661.99	234.57	0.35	8719.72	4100.48	12820.20	0.32	77.27	8.68
10	242.28	45.94	0.19	802.21	468.74	1270.95	0.37	92.63	11.57
Feldspar-2									
10	261.20	73.28	0.28	744.67	605.28	1349.95	0.45	85.25	10.45
20	403.82	118.68	0.29	2191.62	1042.12	3233.75	0.32	83.16	9.02
35	551.95	152.83	0.28	5220.39	2868.81	8089.20	0.35	72.74	8.22
5	176.55	41.54	0.24	272.52	194.49	467.00	0.42	99.34	12.52
50	690.00	209.72	0.30	9602.44	5417.44	15019.87	0.36	62.17	5.98
Dolomite-1									
2	102.49	59.80	0.58	34.02	67.00	101.02	0.66	155.50	10.45
5	183.80	107.66	0.59	144.85	287.24	432.09	0.66	123.00	8.86
10	280.70	102.66	0.37	396.02	919.43	1315.45	0.70	132.57	7.35
20	414.51	233.08	0.56	1191.88	2620.80	3812.67	0.69	114.32	7.26
40	649.37	337.34	0.52	3649.10	8454.46	12103.57	0.70	99.10	6.09
Dolomite-2									
20	415.20	266.86	0.64	1136.12	2660.33	3796.45	0.70	113.13	7.32
35	585.11	383.60	0.66	2636.50	5381.89	8018.38	0.67	103.11	6.59
50	717.39	430.81	0.60	4903.53	9212.99	14116.52	0.65	97.59	6.47
5	183.15	90.46	0.49	146.71	284.59	431.30	0.66	129.21	8.65
10	266.60	138.96	0.52	389.37	854.13	1243.50	0.69	132.11	8.42
Calcite-1									
5	275.12	168.13	0.61	143.88	491.02	634.90	0.77	84.05	3.53
20	598.67	363.55	0.61	1274.37	3537.27	4811.63	0.74	73.07	3.26
35	840.05	550.04	0.65	2761.55	8134.53	10896.08	0.75	74.66	2.76
50	956.49	635.79	0.66	4858.01	13676.13	18534.14	0.74	73.18	3.09
10	418.88	269.25	0.64	438.64	1453.00	1891.64	0.77	75.01	3.17
Calcite-2									
5	292.63	175.64	0.60	154.50	493.91	648.41	0.76	74.14	3.15
20	628.24	419.73	0.67	1261.70	4095.02	5356.72	0.76	68.28	2.97
35	895.33	624.36	0.70	2746.90	9613.55	12360.45	0.78	67.01	2.39
10	439.45	313.23	0.71	377.48	1527.98	1905.46	0.80	77.59	2.83
Clay minerals									
5	450.22	247.32	0.55	290.59	640.83	931.42	0.69	29.13	1.41
50	1459.70	950.00	0.65	7430.76	22056.89	29487.65	0.75	35.77	1.22
10	664.12	366.40	0.55	962.05	2166.29	3128.33	0.69	27.77	1.39
2	277.38	161.50	0.58	75.71	149.41	225.12	0.66	30.55	1.43
0.5	119.10	66.60	0.56	9.26	18.58	27.84	0.67	32.61	1.81

Note: F_m: the indentation load. $h_{max \text{ and }} h_p$: the maximum and residual indentation depth, respectively; W_{elast} and W_{plas}: the elastic work and plastic work, respective; E_s and H_s: the Young's modulus and hardness obtained by quasi-static nanoindentation.
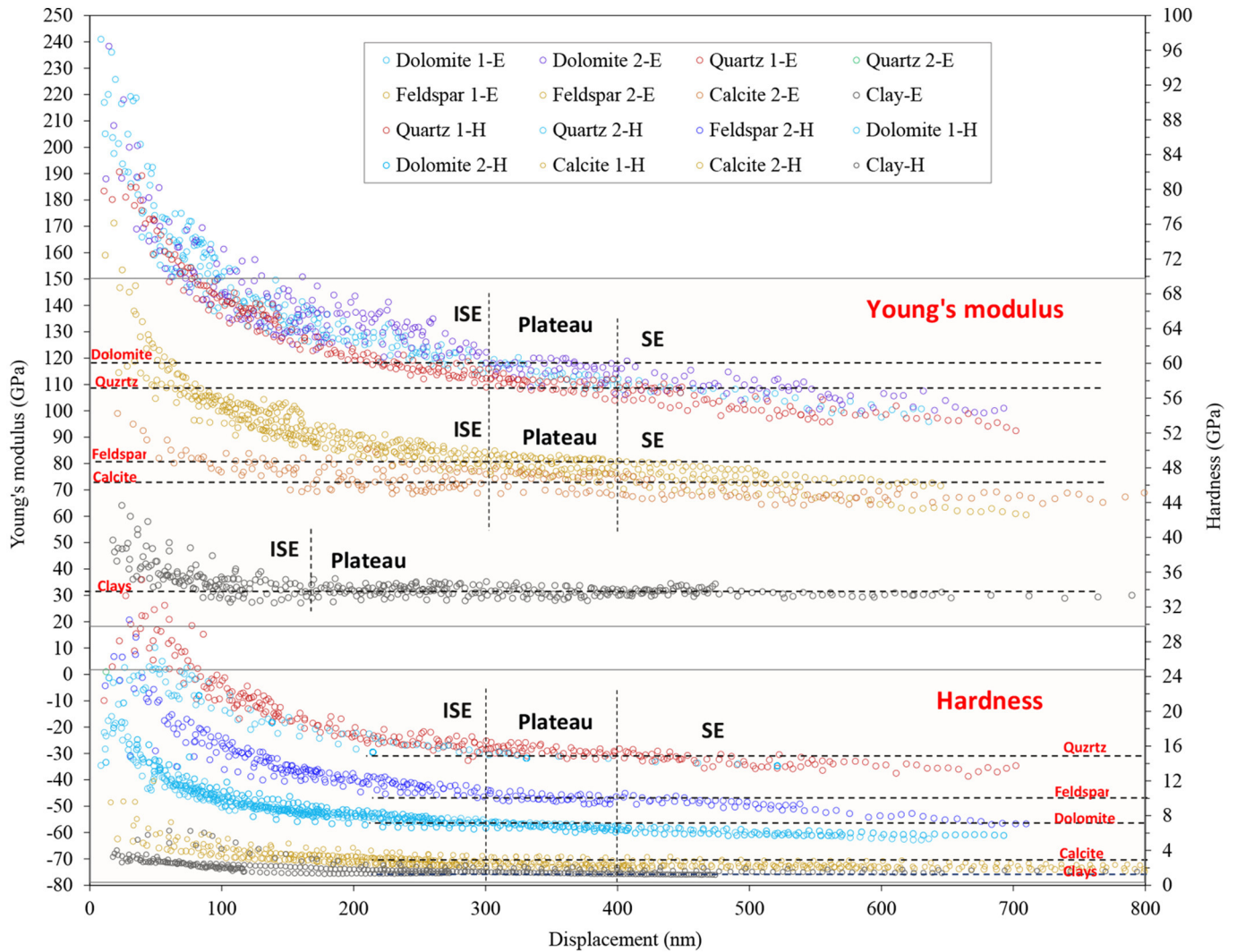

Fig. 11. The depth profiles of Young's modulus and hardness for different shale matrix minerals produced by nano-DMA, showing the indentation size effect (ISE) and substrate effect (SE). The mechanical parameters of clay minerals exhibit a two-stage change, i.e., an initial sharp decline, followed by a plateau, with respect to increase in indentation depth. For the non-clay minerals, the variations in their mechanical parameters exhibit one more stage after the plateau: a slow decrease.

mechanical interactions of individual plate-like clay particles, which also results in the ISE. Resembling the established dislocation density theory for the ISE of a single-phase material, the ISE of a composite material is predicted to stem from the change in packing density resulting from the penetration of the indenter to a different indentation depth. Overall, the ISE of clay composites complete at a depth interval of 120–300 nm, which is relatively smaller than those of non-clay minerals.

At greater indentation depth, the mechanical parameters of non-clay minerals exhibit a slight decrease in varying degrees. Based on a high heterogeneity of shale consisting of various phases that interact with each other, it is likely that the indentation of non-clay minerals was influenced by the underlying softer phases or pressure-bearing framework at a large indentation depth. The optical images provide a description of the shale microstructure as comprising non-clay minerals embedded in clay matrix, the mechanical parameters of which remain unchanged at this indentation depth interval. Accordingly, it can be inferred that the softer clay minerals act as the substrate material of these non-clay minerals. As a result, nanoindentation measures a

composite value depending on the ratio of each component under the probe, and the different decrease amplitudes (expressed as the curve slope) of mechanical parameters among different non-clay minerals at this stage reflect the different mechanical differences between different non-clay minerals and clays. It should be noted that although clay minerals overall act as the pressure-bearing skeleton material in shale, they do not always act as infinitely continuous blocks and sometime behave as locally stacked aggregates. In some cases, the indentation of clay minerals appears to be affected by substrate stiffer phases at a shallow indentation depth (> 450 nm), manifested as a sharp rise in the Young's modulus depth profile after the plateau stage (Fig. 12).

This indentation phenomenon is also called the "substrate effect" (SE) in materials science, and typically occurs in the indentation process of soft film/hard substrate composite materials (e.g. Tian et al., 2002; Ma et al., 2012; Chen, 2012; Chi and Chung, 2003; Guo et al., 2004; Manjunath and Surendran, 2012, 2013). Theoretically, SE is inevitable in the nanoindentation testing of a heterogeneous composite material; however, it can be neglected via obedience to some criteria for selecting indentation depth. Previous studies have suggested that to
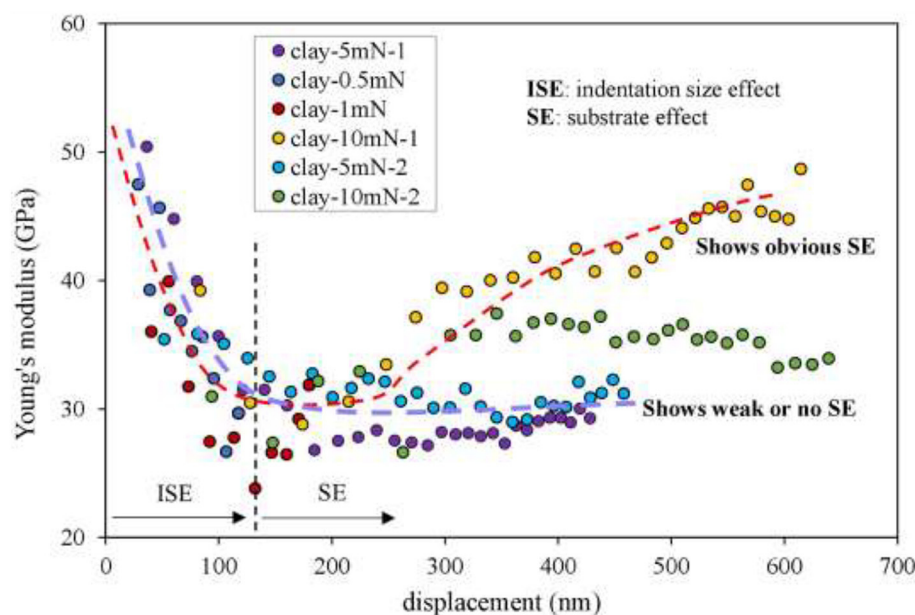
Fig. 12. The occasionally appeared substrate effect (SE) in the indentation process of clay minerals at large indentation depths. When the indentation depth is not more than 450 nm, the Young's modulus depth profile appears a normal two-stage change controlled by the indentation size effect (ISE), i.e., an initial sharp decline, followed by a plateau. When the indentation depth exceeds 600 nm, obvious substrate effect appears in the Young's modulus depth profile, manifested as a sharp rise of Young's modulus after the plateau stage.

characterize the thin film independent of its substrate, indentation depth should be at most 1/10 of the thickness of the film (Perriot and Barthel, 2004). In this study, we found an indentation depth of ~400 nm for different non-clay minerals avoiding the SE, which is 1/100 to 1/50 of the characteristic length scales of tested mineral grains (20–40 μm) observed under the microscope. Such a low ratio indicates that the nanoindentation of the single mineral grains is easily affected by the substrate phases, and also reminds us that a small indentation depth is always preferred even if the minerals to be indented are large-sized. In addition to the possibility that the minerals have inherent high sensitivities to SE, there are other possibilities that may lead to this low ratio. The first is that the indenter penetrates exactly into the minor axis of the mineral crystal, whose thickness in this direction is significantly thinner than the transverse length scale observed under the microscope. The other possibility is that the mechanical polishing process greatly reduces the original thickness of the matrix minerals, thereby causing the indentation process of the indented minerals to be influenced by the substrate phases at a very low depth.

3.4. Measured Young's modulus and hardness

The plateau sections in the mechanical depth profiles reveal with confidence the Young's moduli and hardnesses for calcite, dolomite, quartz, and feldspar, at 70–75 GPa and 2–3 GPa, 115–120 GPa and 7–8 GPa, 105–110 GPa and 14–16 GPa, and 75–85 GPa and 9–10 GPa, respectively. These measured Young's moduli nearly equal those of non-clay minerals, as obtained using indentation on macroscale single crystals (Goldsby et al., 2004; Broz et al., 2006; Whitney et al., 2007). This similarity in values indicates that the methodology used in this study for determining the intrinsic mechanical parameters of shale matrix minerals by virtue of mechanical depth profiles in this study is credible and can be used for other heterogenous composite materials. Additionally, the selected mechanical values from the platform stage are close to those obtained directly from the quasi-static nanoindentation at similar indentation depths (the shaded in Table 2), demonstrating the consistency of dynamic indentation and quasi-static indentation in obtaining mechanical values of indented materials. Notably, these measured Young's moduli of non-clay minerals are obviously higher than the reported moduli in previous studies using the AFM QNM technique (Eliyahu et al., 2015; Emmanuel et al., 2016; Li et al., 2018), demonstrating the advantages of nanoindentation

technology in the characterization of the mechanical properties of shale matrix minerals.

When the mechanical depth profile appears plateaued, the Young's modulus and hardness of clay composites, are approximately 30 GPa and 1.5 GPa, which are near the asymptotic mechanical values extrapolated from porous clay composites in low-maturity shales when the clay packing density is 1.0 (Bobko and Ulm, 2008). Clay packing density describes the microstructure of porous clay composites, and a value of 1.0 describes an ideal state of close packing without pores. Therefore, the high values of Young's modulus and hardness of the clay indicate that the Longmaxi Formation shale is strongly compacted, thus leading to densely packed clay composites, which have been evidenced in previous studies using SEM (Yang et al., 2017b, 2020). It was also noticed that the maximum Young's modulus and hardness values of clay composites obtained in this study are still lower than those obtained by Abedi et al. (2016) through the back-analysis of indentation data of organic/clay mixtures. Given that clays in shale are generally embedded with organic matter, the reason for the lower values may be because this study tested mixtures of clay composites with organic matter. The organic matter generally has lower mechanical values compared to those of clay minerals (Zeszotarski et al., 2004; Kumar et al., 2012; Bennett et al., 2015; Eliyahu et al., 2015), which therefore reduced the Young's modulus and hardness of the clay composites.

4. Conclusions

In view of previous omissions and defects in the mechanical characterization of shale constituents using the traditional quasi-static nanoindentation technique, this study employed a highly distinguishing optical microscope and a newly emerging dynamic nanoindentation technique to perform the mineral-positioned nanoindentation in shale and obtain the mechanical depth profiles of shale-constitutive minerals. The following conclusions can be made:

(1) The resulted load–displacement curves show that the silicates (quartz and feldspar) exhibit high elastic characteristics during nanoindentation with small irrecoverable deformation. Comparatively, the carbonates (calcite and dolomite) and clay minerals demonstrate great plastic characteristics with large irrecoverable deformation. These different mechanical responses among non-clay minerals are a result of differences in their crystal

structures. But for the clay minerals, the significant plastic deformation is actually caused by the mechanical bending and slippage of individual plate-like clay particles within the clay composites under external forces.

(2) Controlled by the ISE, the mechanical parameters of clay minerals exhibit a two-stage change, i.e., an initial sharp decline, followed by a plateau, with respect to the increase in indentation depth. For the non-clay minerals, the variations in their mechanical parameters demonstrate a third stage after the plateau: a slow decrease, which is the result of the interference of softer clay minerals as the matrix pressure-bearing skeleton material. The ISE comes from the adjustment of the internal structure (or texture) of the material in response to the pressing of the indenter, and thus cannot reflect the real mechanical properties of the material. Whereas the platform section represents the indenter overcoming the ISE layer and actually probing the material as it is, the mechanical values measured at this stage are recognized as the true mechanical values for the material.

(3) The depth profiles of mechanical parameters result in a confident conclusion that the ISE nearly disappears at an indentation depth of approximately 200–300 nm for all matrix minerals suitable for indentation testing. In addition, the indentation depth at which SE occurs is related to the thicknesses of the indented minerals, which however cannot be determined under the microscope. Using the characteristic length scales (d) of the minerals observed under the microscope and comparing with the indentation depth at which SE occurs, we determined that the indentation depth should be at most $d/50$ to effectively avoid SE. Therefore, it is recommended that an indentation depth range of $200\ \text{nm} < h < d/50$ be used for obtaining the intrinsic mechanical parameters of shale matrix minerals.

(4) Typical Young's moduli and hardnesses measured in this study include approximately 30 GPa and 1.5 GPa for clay minerals, 105–110 GPa and 14–16 GPa for quartz, 75–85 GPa and 9–10 GPa for feldspar, 70–75 GPa and 2–3 GPa for calcite, and 115–120 GPa and 7–8 GPa for dolomite.

Declaration of Competing Interest

The authors declare that they have no known competing financial interests or personal relationships that could have appeared to influence the work reported in this paper.

Acknowledgments

References

Abedi, S., Slim, M., Ulm, F.J., 2016. Nanomechanics of organic-rich shales: the role of thermal maturity and organic matter content on texture. Acta Geotech. 11 (4), 775–787.

Akono, A.T., Kabir, P., 2016. Nano-scale characterization of organic-rich shale via indentation methods. In: Jin, C., Cusatis, G. (Eds.), New Frontiers in Oil and Gas Exploration. Springer, Cham.

Alkharraa, H., Alameer, A., Alqahtani, F., Alsultan, A., Alabbad, M., Alobaid, O., 2015. Integration of Petrophysical and Geomechanical Properties for Enhanced Fracture Design.

Bass, J.D., 1995. Elasticity of minerals, glasses, and melts. In: Mineral Physics and Crystallography: A Handbook of Physical Constants. vol. 2. pp. 45–63.

Bennett, K.C., Berla, L.A., Nix, W.D., Borja, R.I., 2015. Instrumented nanoindentation and 3D mechanistic modeling of a shale at multiple scales. Acta Geotech. 10, 1–14.

Blackwill, R.D., O'Sullivan, M.L., 2014. America's energy edge. Foreign Affairs 93, 21–22.

Bobko, C., Ulm, F.-J., 2008. The nano-mechanical morphology of shale. Mech. Mater. 40, 318–337.

Broz, M.E., Cook, R.F., Whitney, D.L., 2006. Microhardness, toughness, and modulus of Mohs scale minerals. Am. Mineral. 91, 135–142.

Carter, K.M., Harper, J.A., Schmid, K.W., Kostelnik, J., 2011. Unconventional natural gas resources in Pennsylvania: the backstory of the modern Marcellus shale play. Environ. Geosci. 18 (4), 217–257.

Chen, J., 2012. On the determination of coating toughness during nanoindentation. Surf. Coat. Technol. 206, 3064–3068.

Chi, S.H., Chung, Y.L., 2003. Cracking in coating–substrate composites with multi layered and FGM coatings. Eng. Fract. Mech. 70, 1227–1243.

Constantinides, G., Chandran, K.S.R., Ulm, F.-J., Van Vliet, K.J., 2006. Grid indentation analysis of composite microstructure and mechanics: principles and validation. Mat. Sci. Eng. A 430, 189–202.

Dong, T., Harris, N.B., 2020. The effect of thermal maturity on porosity development in the Upper Devonian–lower Mississippian Woodford Shale, Permian Basin, US: Insights into the role of silica nanospheres and microcrystalline quartz on porosity preservation. Int. J. Coal Geol. 217, 103346.

Dong, T., He, S., Chen, M., Hou, Y., Guo, X., Wei, C., Han, Y., Yang, R., 2019. Quartz types and origins in the paleozoic Wufeng-Longmaxi Formations, Eastern Sichuan Basin, China: Implications for porosity preservation in shale reservoirs. Mar. Pet. Geol. 106, 62–73.

Eliyahu, M., Emmanuel, S., Day-Stirrat, R.J., Macaulay, C.I., 2015. Mechanical properties of organic matter in shales mapped at the nanometer scale. Mar. Pet. Geol. 59, 294–304.

Elmustafa, A.A., Stone, D.S., 2003. Nanoindentation and the indentation size effect: Kinetics of deformation and strain gradient plasticity. J. Mech. Phys. Solids 51 (2), 357–381.

Emmanuel, S., Eliyahu, M., Day-Stirrat, R.J., Hofmann, R., Macaulay, C.I., 2016. Impact of thermal maturation on nano-scale elastic properties of organic matter in shales. Mar. Pet. Geol. 70, 175–184.

Fischer-Cripps, A., 2002. Nanoindentation. Springer-Verlag, New York.

Goldsby, D.L., Rar, A., Pharr, G.M., Tullis, T.E., 2004. Nanoindentation creep of quartz, with implications for rate-and state-variable friction laws relevant to earthquake mechanics. J. Mater. Res. 19 (1), 357–365.

Guo, L., Wu, L., Zeng, T., Ma, L., 2004. The dynamic fracture behaviour of a functionally graded coating–substrate system. Compos. Struct. 64, 433–441.

Hackley, P.C., Cardott, B.J., 2016. Application of organic petrography in north American shale petroleum systems: a review. Int. J. Coal Geol. 163, 8–51.

Kuila, U., Prasad, M., 2013. Specific surface area and pore-size distribution in clays and shales. Geophys. Prospect. 61 (2), 341–362.

Kumar, V., Curtis, M.E., Gupta, N., Sondergeld, C.H., Rai, C.S., 2012. Nano to macro mechanical characterization of shale. In: SPE Annual Technical Conference and Exhibition. Society of Petroleum Engineers.

Li, C., Ostadhassan, M., Guo, S., Gentzis, T., Kong, L., 2018. Application of PeakForce tapping mode of atomic force microscope to characterize nanomechanical properties of organic matter of the Bakken Shale. Fuel 233, 894–910.

Li, C., Ostadhassan, M., Kong, L., Bubach, B., 2019. Multi-scale assessment of mechanical properties of organic-rich shales: a coupled nanoindentation, deconvolution analysis, and homogenization method. J. Pet. Sci. Eng. 174, 80–91.

Liebau, F., Gies, H., Gunawardane, R.P., Marler, B., 1986. Classification of tectosilicates and systematic nomenclature of clathrate type tectosilicates: a proposal. Zeolites 6 (5), 373–377.

Liu, K., Mehdi, O., 2017. Microstructural and geomechanical analysis of Bakken shale at nanoscale. J. Pet. Sci. Eng. 153, 133–144.

Liu, K., Ostadhassan, M., Bubach, B., 2016. Applications of nano-indentation methods to estimate nanoscale mechanical properties of shale reservoir rocks. J. Nat. Gas Sci. Eng. 35, 1310–1319.

Liu, K., Ostadhassan, M., Bubach, B., Ling, K., Tokhmechi, B., Robert, D., 2018. Statistical grid nanoindentation analysis to estimate macro-mechanical properties ofthe Bakken Shale. J. Nat. Gas Sci. Eng. 53, 181–190.

Liu, Y., Xiong, Y., Liu, K., Yang, C., Peng, P., 2019. Indentation size and loading rate sensitivities on mechanical properties and creep behavior of solid bitumen. Int. J. Coal Geol. 216, 103295.

Ma, Z., Zhou, Y., Long, S., Lu, C., 2012. On the intrinsic hardness of a metallic film/substrate: indentation size and substrate effects. Int. J. Plast. 34, 1–11.

Manjunath, G.L., Jha, B., 2019. Geomechanical characterization of gondwana shale across nano-micro-meso scales. Int. J. Rock Mech. Min. 119, 35–45.

Manjunath, G.L., Surendran, S., 2012. Dynamic fracture toughness of coated structural components at different temperatures. In: Proceedings of the ASME 2012 31st International Conference on Ocean, Offshore and Arctic Engineering, OMAE 2012, Rio de Janeiro, Brazil.

Manjunath, G.L., Surendran, S., 2013. Effect of mono and composite coating on dynamic fracture toughness of metals at different temperatures. Compos. Part B- Eng. 51, 359–367.

Mashhadian, M., Verde, A., Sharma, P., Abedi, S., 2018. Assessing mechanical properties of organic matter in shales: results from coupled nanoindentation/SEM-EDX and micromechanical modeling. J. Pet. Sci. Eng. 165, 313–324.

Mavko, G., Mukerji, T., Dvorkin, J., 2009. The Rock Physics Handbook. Cambridge University Press.

Milliken, K.L., Ergene, S.M., Ozkan, A., 2016. Quartz types, authigenic and detrital, in the Upper cretaceous Eagle Ford Formation, South Texas, USA. Sediment. Geol. 273–288.

Nagel, N.B., Sanchez, M.A., Lee, B., 2012. Gas shale hydraulic fracturing: A numerical evaluation of the effect of geomechanical Parameters. In: SPE Hydraulic Fracturing Technology Conference, 6–8 February, the Woodlands, Texas, USA.

Nix, W.D., Gao, H., 1998. Indentation size effects in crystalline materials: a law for strain gradient plasticity. J. Mech. Phys. Solids 46 (3), 411–425.

Oliver, W.C., Pharr, G.M., 1992. An improved technique for determining hardness and elastic modulus using load and displacement sensing indentation experiments. J. Mater. Res. 7, 1564–1583.

Oliver, W.C., Pharr, G.M., 2004. Measurement of hardness and elastic modulus by instrumented indentation: advances in understanding and refinements to methodology. J. Mater. Res. 19 (1), 3–20.

Perriot, A., Barthel, E., 2004. Elastic contact to a coated half-space: Effective elastic modulus and real penetration. J. Mater. Res. 19 (2), 600–608.

Pharr, G.M., Herbert, E.G., Gao, Y., 2010. The indentation size effect: a critical examination of experimental observations and mechanistic interpretations. Annu. Rev. Mater. Res. 40, 271–292.

Pittenger, B., Erina, N., Su, C., 2014. Mechanical property mapping at the nanoscale using PeakForce QNM scanning probe technique. In: Nanomechanical Analysis of High Performance Materials. Springer, Dordrecht, pp. 31–51.

Schuh, C.A., 2006. Nanoindentation studies of materials. Mater. Today 9, 32–40.

Shi, X., Jiang, S., Lu, S., He, Z., Li, D., Wang, Z., Xiao, D., 2019. Investigation of mechanical properties of bedded shale by nanoindentation tests: a case study on lower Silurian Longmaxi Formation of Youyang area in Southeast Chongqing, China. Pet. Explor. Dev. 46 (1), 163–172.

Tian, J., Han, Z., Lai, Q., Dai, J., Li, G., 2002. A two-step penetration method for the correct measurement of the mechanical properties of hard coatings. J. Func. Biomater. 33 (4), 384–386.

Trtik, P., Kaufmann, J., Volz, U., 2012. On the use of peak-force tapping atomic force microscopy for quantification of the local elastic modulus in hardened cement paste. Cem. Concr. Res. 42, 215–221.

Ulm, F.-J., Constantinides, G., van Vliet, K.J., 2003. On the use of nanoindentation for cementitious materials. Mater. Struct. 36 (257), 191–196.

Whitney, D.L., Broz, M., Cook, R.F., 2007. Hardness, toughness, and modulus of some common metamorphic minerals. Am. Mineral. 92 (2–3), 281–288.

Wilson, M.J., Shaldybin, M.V., Wilson, L., 2016a. Clay mineralogy and unconventional hydrocarbon shale reservoirs in the USA. I. Occurrence and interpretation of mixed-layer R3 ordered illite/smectite. Earth-Sci. Rev. 158, 31–50.

Wilson, M.J., Wilson, L., Shaldybin, M.V., 2016b. Clay mineralogy and unconventional hydrocarbon shale reservoirs in the USA. II. Implications of predominantly illitic clays on the physico-chemical properties of shales. Earth-Sci. Rev. 158, 1–8.

Yang, Z., Wang, L., Zhang, G., Ho, C., 2016. Micromechanical characterization of fluid-shale interactions via nanoindentation. In: SPE Asia Pacific Hydraulic Fracturing Conference. Society of Petroleum Engineers.

Yang, J., Hatcherian, J.J., Hackley, P.C., Pomerantz, A.E., 2017a. Nanoscale geochemical and geomechanical characterization of organic matter in shale. Nat. Commun. 8 (1), 1–9.

Yang, C., Zhang, J., Tang, X., Ding, J., Zhao, Q., Dang, W., Chen, H., Su, Y., Li, B., Lu, D., 2017b. Comparative study on micro-pore structure of marine, terrestrial, and transitional shales in key areas, China. Int. J. Coal Geol. 171, 76–92.

Yang, C., Xiong, Y., Zhang, J., 2020. A comprehensive re-understanding of the OM-hosted nanopores in the marine Wufeng–Longmaxi shale formation in South China by organic petrology, gas adsorption, and X-ray diffraction studies. Int. J. Coal Geol. 218, 103362.

Zhang, F., Guo, H., Hu, D., Shao, J., 2018. Characterization of the mechanical properties of a claystone by nano-indentation and homogenization. Acta Geotech. 13, 1395–1404.

Zhao, J., Jin, Z., Jin, Z., Hu, Q., Hu, Z., Du, W., Yan, C., Geng, Y., 2017. Mineral types and organic matters of the Ordovician-Silurian Wufeng and Longmaxi Shale in the Sichuan Basin, China: Implications for pore systems, diagenetic pathways, and reservoir quality in fine-grained sedimentary rocks. Mar. Pet. Geol. 86, 655–674.

Zeszotarski, J.C., Chromik, R.R., Vinci, R.P., Messmer, M.C., Michels, R., Larsen, J.W., 2004. Imaging and mechanical property measurements of kerogen via nano indentation. Gepchim. Cosmochim. Ac. 68, 4113–4119.

Zhu, W., Hughes, J., Bicanic, N., Pearce, C.J., 2007. Nanoindentation mapping of mechanical properties of cement paste and natural rocks. Mater. Charact. 58 (11), 1189–1198.